nature materials

Article

https://doi.org/10.1038/s41563-024-01838-8

Inverse chirality-induced spin selectivity effect in chiral assemblies of π-conjugated polymers

Received: 2 February 2023

Accepted: 14 February 2024

Published online: 15 March 2024

Check for updates

Rui Sun[1,7], Kyung Sun Park[2,7], Andrew H. Comstock[1], Aeron McConnell[1], Yen-Chi Chen[2], Peng Zhang[3], David Beratan[3], Wei You[4], Axel Hoffmann[5], Zhi-Gang Yu[6], Ying Diao[2] ✉ & Dali Sun[1] ✉

Coupling of spin and charge currents to structural chirality in non-magnetic materials, known as chirality-induced spin selectivity, is promising for application in spintronic devices at room temperature. Although the chirality-induced spin selectivity effect has been identified in various chiral materials, its Onsager reciprocal process, the inverse chirality-induced spin selectivity effect, remains unexplored. Here we report the observation of the inverse chirality-induced spin selectivity effect in chiral assemblies of π-conjugated polymers. Using spin-pumping techniques, the inverse chirality-induced spin selectivity effect enables quantification of the magnitude of the longitudinal spin-to-charge conversion driven by chirality-induced spin selectivity in different chiral polymers. By widely tuning conductivities and supramolecular chiral structures via a printing method, we found a very long spin relaxation time of up to several nanoseconds parallel to the chiral axis. Our demonstration of the inverse chirality-induced spin selectivity effect suggests possibilities for elucidating the puzzling interplay between spin and chirality, and opens a route for spintronic applications using printable chiral assemblies.

Reversible conversion between charge and spin currents in the solid state leads to a new paradigm for spintronics[1–3]. One prototypical example is the spin Hall effect (SHE)[4,5] and its reciprocal process, the inverse spin Hall effect (ISHE)[6,7]. The SHE describes how a flow of longitudinal charge current $\mathbf{J}_c$ in a non-magnetic material can generate a transverse spin current $\mathbf{J}_s$ (ref. 4). Following the Onsager relation, the ISHE describes how a longitudinal spin current can generate a transverse charge current[6]. The SHE/ISHE can be quantified with the coefficient of spin-charge interconversion as represented by the spin Hall angle ($\theta_{sh} \equiv \mathbf{J}_s/\mathbf{J}_c$) which is proportional to the strength of intrinsic spin–orbit coupling (SOC) in non-magnetic materials as demonstrated in inorganic materials[7] and organic semiconductors[8]. The SHE/ISHE has been recently employed as a powerful tool for material characterization[9–11] and for the generation and detection of spin current for advanced spintronic devices[12–14].

Chiral materials have recently presented a new platform for the pursuit of promising research on spin current generation by harnessing symmetry beyond the intrinsic SOC. Chirality is a structural property of a system with broken inversion symmetry. Structural chirality has emerged in direct conjunction with spin current generation even in

[1]Department of Physics and Organic and Carbon Electronics Lab (ORaCEL), North Carolina State University, Raleigh, NC, USA. [2]Department of Chemical and Biomolecular Engineering, University of Illinois at Urbana-Champaign, Urbana, IL, USA. [3]Department of Chemistry, Duke University, Durham, NC, USA. [4]Department of Chemistry, University of North Carolina at Chapel Hill, Chapel Hill, NC, USA. [5]Department of Materials Science & Engineering and Materials Research Laboratory, University of Illinois at Urbana-Champaign, Urbana, IL, USA. [6]Sivananthan Laboratories, Bolingbrook, Illinois, USA. [7]These authors contributed equally: R. Sun, K. S. Park. ✉e-mail: yingdiao@illinois.edu; dsun4@ncsu.edu

https://doi.org/10.1038/s41563-024-01838-8

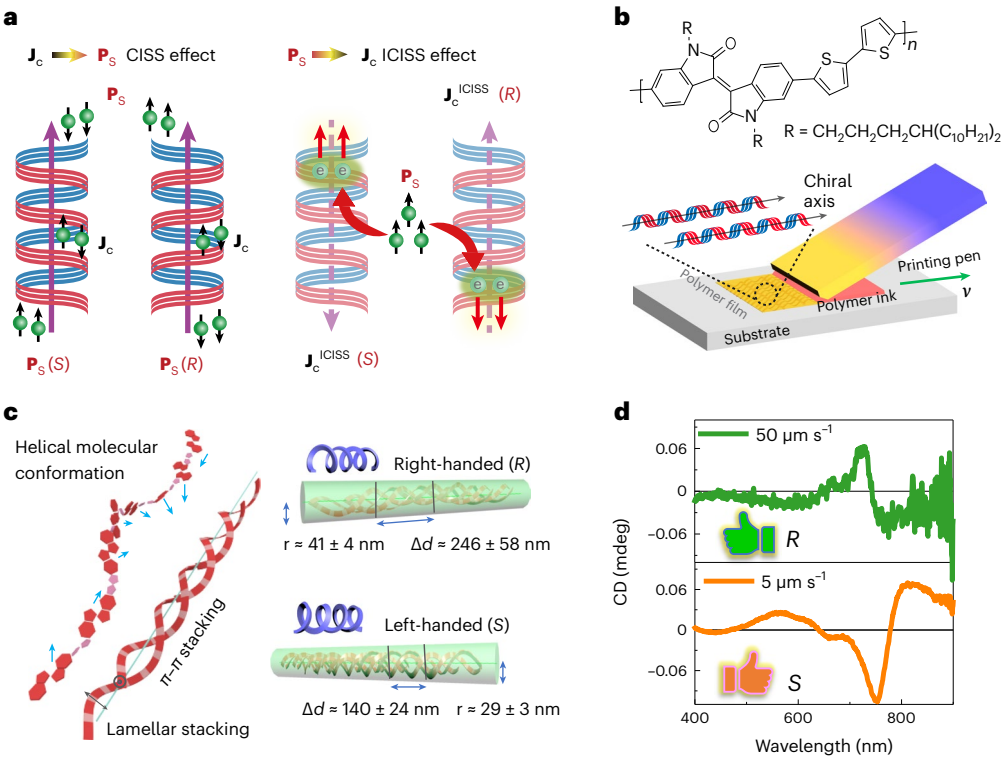

Fig. 1 | Schematic illustrations of CISS, ICISS and chirality formation in π-conjugated PII2T polymers. a, In the CISS effect, a flow of charge current $\mathbf{J}_c$ in the *R*(*S*)-chiral structure generates a pair of spin polarizations $\mathbf{P}_S$ parallel and antiparallel to the chiral axis[19]. The reciprocal process of CISS, the ICISS effect, describes how the spin polarization $\mathbf{P}_S$ parallel (or antiparallel) to the chiral axis produces a charge current $\mathbf{J}_c$ of which the flow direction is determined by the chirality. **b**, Chemical structure of PII2T system and the schematic diagram of helical structure accessed via blade printing. **c**, A sketch of the inferred flow-controlled chiral structure. The torsional PII2T assembles in a twisted or bent fashion locked in by π–π and lamellar stacking (molecular scale, represented by red ribbon). The twisted PII2T molecules form helical fibres having *R* or *S* handedness (nanoscale, inside the green shell). r and Δd refer to the radius and pitch length of the helical fibres. **d**, Obtained CD of PII2T polymers at different printing speeds v. The viscous force varies with v and gives rise to the chirality modulation from *S* handedness (v = 5 μm s^{-1}, yellow) to *R* handedness (v = 50 μm s^{-1}, green). Panel **c** adapted with permission from ref. 36, Springer Nature Limited.

the absence of the intrinsic SOC[15,16]. This unique interplay of chirality and spin gives rise to a different type of charge-to-spin conversion, known as the chirality-induced spin selectivity (CISS) effect[15–18], which was first demonstrated in double-stranded deoxyribonucleic acid (DNA) structures (Fig. 1a, left panel). In the CISS effect, a charge current $\mathbf{J}_c$ flowing through a chiral material can generate a pair of spin polarization $\mathbf{P}_S$ that are parallel and antiparallel to the chiral axis and switch polarity depending on the exhibited *R*(*S*) handedness (left- and right-handedness, designated as *S* or *R*, respectively)[19]. The CISS effect reveals a chirality-dependent charge-to-spin conversion in the longitudinal configuration ($\mathbf{P}_S \parallel \mathbf{J}_c$) that cannot be explained by the weak intrinsic SOC reported in hydrocarbon-based chiral compounds composed of light elements. While manifestations of the CISS effect in different chiral materials have launched a wide variety of CISS-related device applications, for example, chiral light control[20–22], magnetoresistance[23–25], magnetism[26,27], quantum computing applications[28–30] and so on, a missing piece is its Onsager reciprocal process, the inverse CISS (ICISS) effect, in organic compounds, which so far has been demonstrated only in inorganic chiral dichalcogenide crystals[31].

Here we report the observation of the ICISS effect in chiral assemblies of a common, achiral π-conjugated organic polymer. The chirality arises from helical supramolecular assemblies of polymers rather than chiral centres in the molecular structure. The ICISS effect is depicted as a flow of spin polarization $\mathbf{P}_S$ parallel or antiparallel to the chiral axis, which is converted into a longitudinal charge current $\mathbf{J}_c$ (Fig. 1a)[31]. Using the spin-pumping approach[10], the amplitudes of the injected spin polarization and output charge current are measured, and the coefficients of the chirality-driven longitudinal spin-to-charge (StC) conversion are characterized. Thanks to the ease of using a large molecular design space and processing via solution printing methods, the precise tuning of helical structures enables a large modulation of spin and carrier transport properties in the chiral assemblies of π-conjugated polymers[32,33]. These advantages provide an ideal platform to reveal the fundamental structure–property relationship in the context of the CISS effect.

Printing chiral thin films of conjugated polymers

Chiral structures of π-conjugated polymer films were prepared with an isoindigo–bithiophene-based copolymer (PII2T). Although the PII2T monomer is achiral, one alluring feature is its achiral-to-chiral transition through evaporative assembly, in which the twisted and bent intramolecular conformation and the staggered intermolecular stacking enable the formation of chiral helical nanofibres[34]. By leveraging the solution printing process, precise control of handedness becomes accessible in printed thin films (Fig. 1b–d). Through the meniscus-guided printing method, the polymer ink solution is sandwiched between a moving blade and a stationary substrate (Fig. 1b). As the solvent evaporates, the polymer assembles to deposit a thin film at the moving, drying meniscus[35]. Consequently, PII2T polymer thin films with opposite handedness can be selectively achieved by varying the printing speed (Supplementary Fig. 1 and 2). Besides controlling handedness, the printing approach can enable the tuning of the chiral helical pitch while attaining a high degree of chiral-axis alignment in the printed films (details in Supplementary Section I.).

https://doi.org/10.1038/s41563-024-01838-8

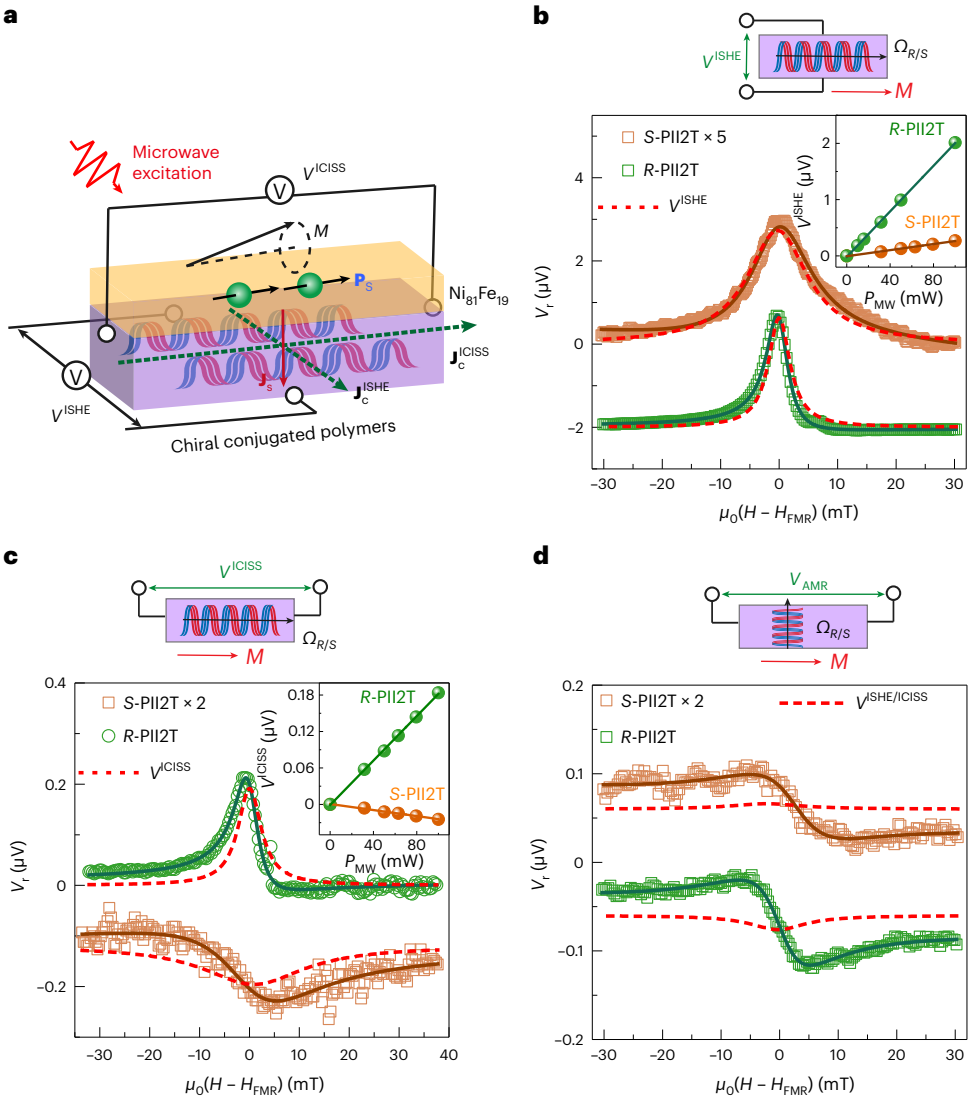

Fig. 2 | ISHE and ICISS effects in chiral polymers. a, Schematic illustration of the ISHE and ICISS measurements in an *R*(*S*)-PII2T/$Ni_{81}Fe_{19}$ device via the spin-pumping method under microwave excitation. **b**,**c**, Field dependence of voltage response (V_r) measured in *R*- and *S*-PII2T/$Ni_{81}Fe_{19}$ devices when the voltage probe direction is perpendicular (configuration **b**, V^{ISHE}) and parallel (configuration **c**, V^{ICISS}) to the chiral axis, $\Omega_{R/S}$. The inset shows the microwave power dependence of $V^{ISHE/ICISS}$. The values of resonance fields in each curve can be found in Supplementary Fig. 11e. The plots are shifted vertically for clarity. **d**, Field dependence of V_{AMR} in both the *R*- and *S*-PII2T/$Ni_{81}Fe_{19}$ devices when the magnetic field and voltage probe are both perpendicular to the chiral axis, showing typical antisymmetric voltage components that can be attributed to the AMR effect. The top image in each panel **b**–**d** illustrates one of three spin-pumping configurations, with a transverse voltage probe (**b**) or a longitudinal probe (**c** and **d**). The dashed lines in each panel show the obtained symmetric voltage component in each curve. The solid lines are fitting curves from Supplementary Information equation (6). μ_0 is the vacuum permeability. All the spin-pumping measurements were carried out at room temperature at microwave frequency, $f = 6$ GHz with $P_{MW} = 100$ mW.

Figure 1d shows the circular dichroism (CD) spectra of the PII2T thin films printed at 5 μm s^{-1} and 50 μm s^{-1}. The opposite CD signals in the wavelength range of 700–800 nm demonstrate the opposite chirality obtained in the *R*(*S*)-PII2T films. Below we refer to the films showing a negative CD signal as *S*-PII2T (printed at 5 μm s^{-1}) while the film having the positive CD signal is defined as *R*-PII2T (printed at 50 μm s^{-1}). The surface morphology and nanoscale helical structure of the thin films, including pitch lengths Δ*d* and radius r of the fibres, are examined by atomic force microscopy (Supplementary Section I). The twisted nanoscale fibres have a helical pitch length of 140 ± 24 nm and a radius of 29 ± 3 nm for the *S*-PII2T film, compared to a helical pitch length of 246 ± 58 nm and a radius of 41 ± 4 nm for the *R*-PII2T film (Fig. 1c, right), which is consistent with our previous work[36]. The modulation of the helical pitch arises from the modulation of backbone torsion at the molecular scale, where a larger pitch length corresponds to a less torsional backbone printed at higher speeds (Supplementary Figs. 4 and 5). The developed printing method also enables a high degree of alignment of the chiral axis over the entire film due to directional mass transport along the printing direction with a narrow orientation distribution of ~15° and ~35° for the *R*-PII2T and *S*-PII2T samples, respectively (Supplementary Fig. 6). Printed films with high degrees of control over handedness, chiral helical pitch and chiral-axis alignment provide an ideal platform to study the ICISS effect.

Inverse chirality-induced spin selectivity effect

We investigated both the ISHE and ICISS effects in *R*- and *S*-PII2T thin films using spin-pumping methods. A 15 nm ferromagnetic $Ni_{81}Fe_{19}$ layer was deposited onto the chiral polymer thin films via electron-beam evaporation ($Ni_{81}Fe_{19}$/PII2T/glass; Methods). Ferromagnetic resonance (FMR) measurement characterizes the magnetic dynamic responses of

https://doi.org/10.1038/s41563-024-01838-8

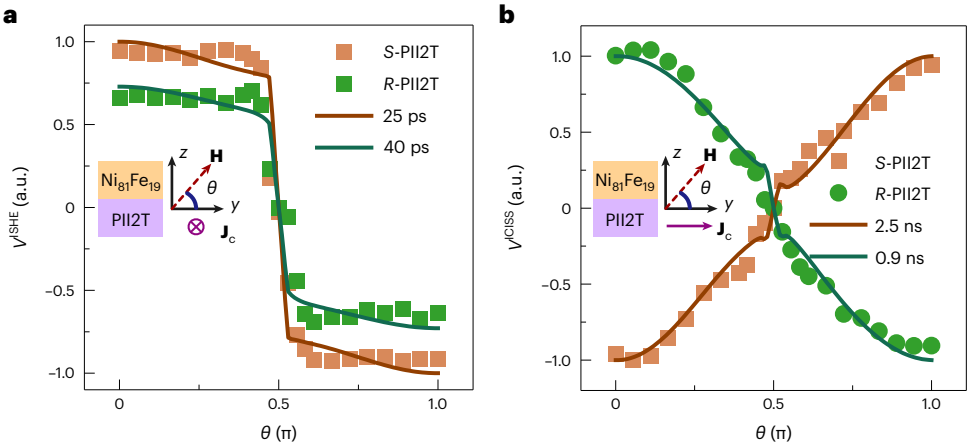

Fig. 3 | Hanle effect under oblique magnetic field. a, The θ dependence of the V^{ISHE} response ($J_c \perp y$, chiral axis $\Omega_{R/S} \parallel y$) measured in *R*-PII2T (green) and *S*-PII2T (orange) devices by applying the oblique magnetic field, **H**, of which the direction is tilted to the out-of-plane direction θ with respect to the *y* axis. **b**, The θ dependence of the V^{ICISS} response ($J_c \parallel y$, chiral axis $\Omega_{R/S} \parallel y$), from which an unprecedented long spin lifetime τ_s of up to the nanosecond timescale is derived from the ICISS process, in sharp contrast to that of the ISHE process in the same device. Solid lines in each panel are the fitted curves using the extended spin Hanle model (Supplementary Information equations (11)–(15)). The microwave frequency is fixed at 6 GHz with a power of 100 mW.

the ferromagnetic layer at different microwave frequencies, from which the resonance field H_{FMR} and the half-width at half-maximum line-width ΔH versus microwave frequency f can be obtained (Supplementary Fig. 11b,c). Under the FMR condition, the magnetization precession of $Ni_{81}Fe_{19}$ injects a pure spin polarization into the PII2T films[9]. A highly enhanced damping factor exists for the *S*-PII2T film as compared to the *R*-PII2T film (Supplementary Fig. 11d). Since PII2T comprises only light elements, the conventional SOC would be negligible and should lead to only moderate damping enhancement[37]. The measured damping enhancement implies the presence of chirality-induced unconventional SOC (uSOC) arising from the helical structure of the polymers[38], leading to the ICISS effect that will be discussed later.

Figure 2b shows the obtained ISHE voltage, V^{ISHE} as a function of applied magnetic field, **H**, for both *S*- and *R*-PII2T/$Ni_{81}Fe_{19}$ devices[39]. The V^{ISHE} is detected perpendicular to the magnetization *M* and chiral axis $\Omega_{R/S}$, that is, $V^{ISHE} \perp M$ and $V^{ISHE} \perp \Omega_{R/S}$ (first probe configuration). The obtained voltage response can be decomposed into a symmetric component, V_S and an asymmetric component, V_A (Supplementary Information equation (6)). The asymmetric part is a side effect from the ferromagnetic layer that can be attributed to anisotropic magnetoresistance (AMR) and the anomalous Hall effect (AHE)[39]. The dominant symmetric component from ISHE (red dotted lines), V^{ISHE} reverses its polarity when the magnetic field is reversed since $V^{ISHE} \propto \mathbf{J}_s \times \mathbf{P}_S(M)$ (Supplementary Fig. 11e). The magnitude of V^{ISHE} in the *R*-PII2T device compares favourably with that measured in the heavy metal (reference sample Pt/$Ni_{81}Fe_{19}$ in Supplementary Fig. 11e) although no heavy elements exist in the chiral polymers. The magnitude of V^{ISHE} in the *S*-PII2T device is weaker due to the different carrier mobilities in the two types of polymers. Both the *S*- and *R*-PII2T devices exhibit the same voltage polarity along +**H**, implying a positive sign of θ_{sh} in both polymers like that of the Pt layer (Supplementary Section III). The magnitude of V^{ISHE} in the two samples exhibits a linear dependence of applied microwave power, P_{MW} (Fig. 2b, inset), consistent with the regular ISHE process[9,10].

The ICISS effect occurs when the spin polarization is converted into an electric current $\mathbf{J}_c^{ICISS}$ parallel or antiparallel to the chiral axis and spin polarization vector, $\mathbf{P}_S$, as illustrated in Fig. 2c. A d.c. electric voltage, V^{ICISS} (the symmetric component of V_r) is detected in the second probe configuration when $V^{ICISS} \parallel M$ and $V^{ICISS} \parallel \Omega_{R/S}$. Figure 2c exhibits the field dependence of the V^{ICISS} response in the *S*- and *R*-PII2T devices under +**H** magnetic field. The V^{ICISS} response is observed in each device, possessing a positive sign for the *R*-PII2T device but a negative sign for the *S*-PII2T device. The voltage polarity of the V^{ICISS} responses in both devices are inverted when the magnetic field is reversed to −**H** (Supplementary Fig. 12). We found that V^{ICISS} manifests as $V^{ICISS} \propto \Omega_{R/S} P_S$ where the value of $\Omega_{R/S}$ represents the polarity of ICISS ($\Omega = +1$ and -1 for *R* and *S* handedness, respectively). This is direct proof of the ICISS effect, whose voltage polarity solely depends on the handedness of films. The inset in Fig. 2c depicts the P_{MW} dependence of V^{ICISS} for *S*- and *R*-PII2T devices. The linear response confirms the spin-pumping process to detect the ICISS effect, which is also consistent with the transfer current–voltage (*I*–*V*) curve measured in the low voltage range (Supplementary Fig. 14). In the current ICISS detection configuration, the regular ISHE response V^{ISHE} should be roughly zero since the voltage probe direction is parallel to the magnetization. However, a residual V^{ISHE} signal induced by unintentional sample misalignment between the magnetic field and voltage probe direction (Supplementary Section V) might remain. To separate this contribution, the V^{ICISS} response is validated by rotating the devices at different in-plane angles φ_H (−5°, 0° and 5°) with respect to **H**. Under this condition, the residual V^{ISHE} reverses polarity since $V^{ISHE} \propto \sin\varphi_H$, whereas the polarity of V^{ICISS} will remain unchanged. No sign change of V^{ICISS} was observed, suggesting that the pronounced ICISS effect dominates the voltage signals and the residual V^{ISHE} is suppressed in the chiral devices (Supplementary Fig. 22a). To further validate that the ICISS effect is solely induced by the structural chirality of the PII2T thin film, we conducted control experiments in the third probe configuration (Fig. 2d). The voltage probe direction is aligned along with the magnetic field, **H** but perpendicular to the chiral axis of the chiral film ($V_r \parallel M$ and $V_r \perp \Omega_{R/S}$). The field dependence of the voltage responses measured in both *R*- and *S*-PII2T devices shows a zero symmetric component from V^{ISHE} and V^{ICISS}, overshadowed by a weak asymmetric component (V_{AMR}).

Combining the data from all three probe configurations, the ICISS effect arises from the spin polarization direction oriented along the chiral axis whose polarity is chirality dependent (Supplementary Fig. 24 and 25). The ICISS effect shares its main features with those reported for the CISS demonstrations[31], that is, an efficient StC conversion in the longitudinal configuration ($\mathbf{P}_S \parallel \mathbf{J}_c$) governed by the uSOC in sharp contrast to the StC conversion in the transverse configuration ($\mathbf{P}_S \perp \mathbf{J}_c$) via ISHE produced by the ordinary SOC.

Hanle effect

The demonstration of the ICISS effect also enables us to probe the spin lifetime in the CISS/ICISS process, which remains unresolved in most

https://doi.org/10.1038/s41563-024-01838-8

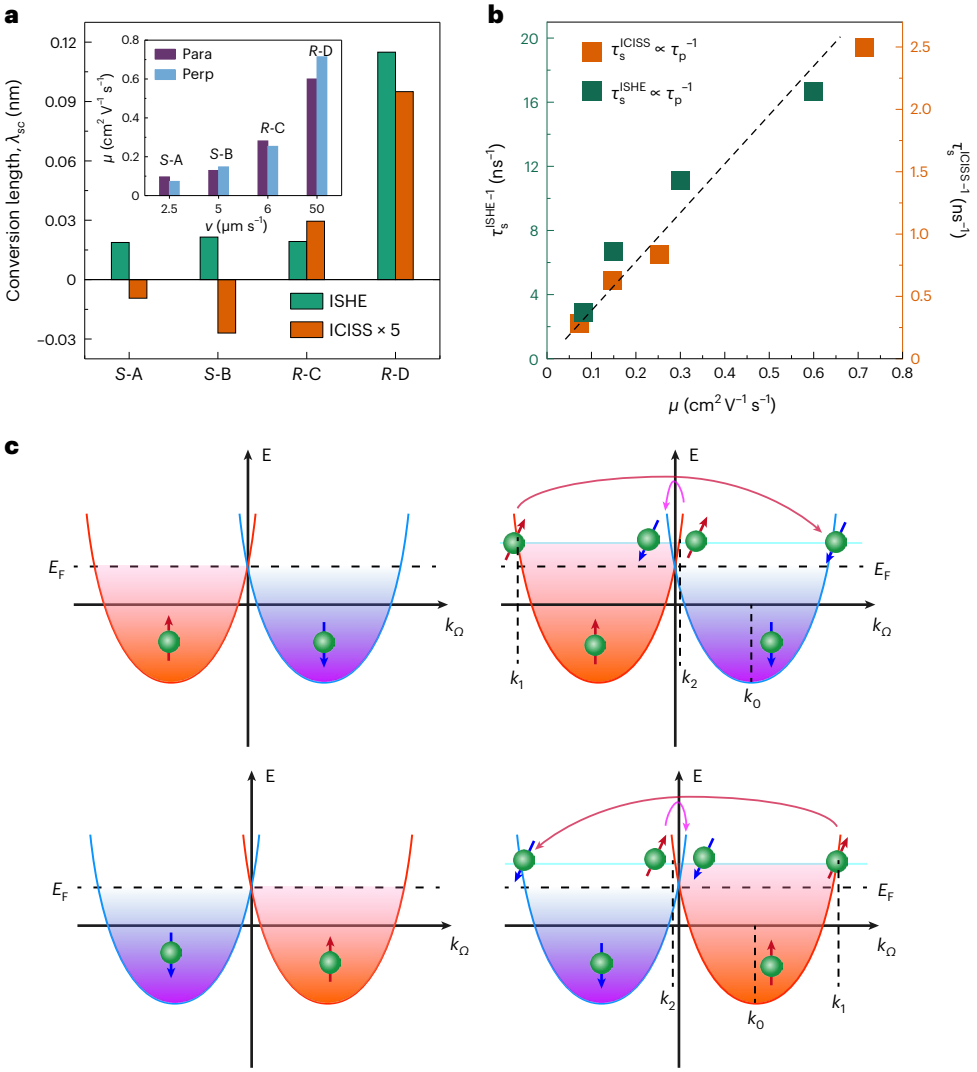

Fig. 4 | Interplays of StC conversion coefficient, carrier mobility and spin relaxation time in chiral PII2T polymers. a, A summary of the StC conversion coefficients, that is, conversion length, λ_{sc} measured from ISHE (green) and ICISS (orange) effects in different chiral polymers with varied mobilities. The inset shows the obtained mobilities in each polymer prepared by different printing speeds (*S*-A(B) and *R*-C(D)). Para (Perp) represents the probe direction of mobility parallel (perpendicular) to the chiral axis. **b**, Correlations between τ_s^{-1} from ISHE (left axis) and ICISS (right axis) and mobilities (μ) show that τ_s^{-1} scales linearly with mobility and momentum scattering time, τ_p. **c**, Schematic diagrams of the proposed chirality-induced spin-momentum locking in energy dispersion relation E(k_Ω), in the presence of the uSOC and the inverted polarity of the ICISS effect in *S*-PII2T (top) and *R*-PII2T (bottom) polymer caused by the spin-flip transition. The curved arrows represent the scattering process between specified k_i (i = 1, 2) states. E_F is the Fermi level.

CISS demonstrations[21,31,40,41]. We conducted spin-pumping measurements at different out-of-plane magnetic field angles θ, to observe an effect named the 'oblique Hanle effect'. It's a typical feature of the observed voltage responses originating from the spin injection from the ferromagnetic layer[42]. When the magnetic field **H** is tilted from the in-plane direction towards the out-of-plane direction, the injected spin polarization $\mathbf{P}_S$ into the chiral polymer layer begins to precess due to the misalignment between the magnetization **M** and **H** in the presence of the large demagnetization magnetic field (up to ~1 T) of $Ni_{81}Fe_{19}$. For the regular ISHE response, the measured voltage direction (along the x direction) is perpendicular to the magnetic field **H** (along the y direction). The y-polarized component of the injected spin polarization dephases due to the Hanle precession, resulting in a modified $V^{ISHE}(\theta)$ curve from which the spin lifetime τ_s can be determined[42,43].

Figure 3a presents the measured θ-dependent V^{ISHE} in the *S*- and *R*-PII2T devices (both films are printed at 10 μm s^{-1} but exhibit opposite chirality) using the ISHE probe configuration. At high θ values, the y-polarized spin component senses a larger out-of-plane magnetic field, which reduces the spin polarization. The reduction of the V^{ISHE} value follows the typical angular dependence, which can be produced well using Supplementary Information equations (10)–(12) (ref. 42). We found that the spin lifetime, τ_s^{ISHE}, from the fitted $V^{ISHE}(\theta)$ curves, is slightly different ($\tau_s^{ISHE} = 25 \pm 5$ ps in *S*-PII2T and 40 ± 10 ps in *R*-PII2T) and varies dramatically when the printing speed changes. It is surprising to obtain different spin relaxation times given that all the PII2T polymer thin films are composed of identical and primarily light elements that should have a small but same conventional SOC responsible for the spin scattering (more details in Supplementary Fig. 17 and Supplementary Table III). This result could be intimately tied to the chirality-induced uSOC arising from the helical curvature of the molecule surface where π- and σ-orbit electrons of carbons are mixed[8,38,44], as corroborated by the changes of damping factors and spin-mixing conductances at the polymer–ferromagnetic interface obtained from the FMR measurements (Supplementary Fig. 11).

Figure 3b shows the θ-dependent symmetric component, V^{ICISS} using the ICISS probe configuration. Both *R*- and *S*-PII2T devices exhibit a more gradual variation of V^{ICISS} at higher field angles compared to that in the ISHE probe configuration. The sign of the line shape is inverted, depending on their chirality. Due to the Hanle effect, the *y* component of injected spin polarization P_S precesses along the oblique magnetic field, **H**, resulting in a variation of V^{ICISS}, which can be described as follows (Supplementary Section V):

$$V^{ICISS}(\theta) \propto P_S^0\left[\cos\theta\cos(\theta-\theta_M)\int_0^d e^{-\frac{z}{\lambda_s}}dz\right] + P_S^0\left[\sin\theta\sin(\theta-\theta_M)\int_0^d \mathrm{Re}\left[e^{-\frac{z}{\lambda_\omega}}\right]dz\right] \quad (1)$$

where P_S^0 is the spin polarization density injected into the PII2T at the interface; θ_M is the angle between the magnetic moment and the *y* direction under the oblique field; *d* is the thickness of the PII2T layer; λ_s is the spin diffusion length along the *z* direction using the spin diffusion model[42]; $\lambda_\omega = \lambda_s/\sqrt{1+i\omega_L\tau_s}$; and $\omega_L = \gamma_c H_{FMR}$ where γ_c is the gyromagnetic ratio of electron and H_{FMR} is the resonance field. An extra longitudinal ISHE signal may be added to the V^{ICISS} response under the oblique field due to the precessed spin polarization component along the *x* direction (Supplementary Section IV) that is given by $V_{ISHE}^{L}(\theta) \propto P_S^0|\sin(\theta-\theta_M)|\int_0^d \mathrm{Im}\left[e^{-\frac{z}{\lambda_\omega}}\right]dz$. The calculated curves from both ISHE and ICISS responses are shown in Supplementary Fig. 19. The measured $V_{ISHE}^{L}(\theta)$ follows an 'M' line shape as seen from the control sample $Ni_{81}Fe_{19}$/Pt in Supplementary Fig. 21, in sharp contrast to our ICISS results in Fig. 3b, indicating that the ISHE contribution in the measured ICISS response is negligibly small. The calculated $V^{ICISS}(\theta)$ in both devices using equation (1) is shown in Fig. 3b, from which the spin relaxation time τ_s^{ICISS} via the ICISS channel can be extracted. The solid curves represent the best fit obtained with $\tau_s^{ICISS} = 0.9 \pm 0.1$ ns for the *R*-PII2T device and $\tau_s^{ICISS} = 2.5 \pm 0.5$ ns for the *S*-PII2T device. Contrary to the much shorter $\tau_s^{ISHE} \approx 40$ ps from the ISHE channel in the same device, the obtained τ_s of several nanoseconds in the ICISS channel is comparable with that in topological materials with spin-momentum locking[45], suggesting a unique spin relaxation caused by the chirality-induced uSOC.

Correlations between spin and charge transport

Observation of the ICISS effect and spin lifetime enables us to precisely quantify the StC conversion efficiency for the ICISS process in the chiral polymer model systems. A series of spin-pumping experiments were performed in polymer thin films whose mobilities and handedness were systematically modulated by varying printing speeds (labelled as *S*-A and *S*-B (*S*-PII2T printed at 5 μm s^{-1}), and *R*-C and *R*-D (*R*-PII2T printed at 50 μm s^{-1}); Methods and Supplementary Fig. 1 and 2). In terms of the characterization of the StC conversion efficiency, we use the conversion length, $\lambda_{sc} = J_c^{2D}/P_S^0$ that is equivalent to $\lambda_{sc} \equiv \theta_{sh}\lambda_s$ (J_c^{2D} is the nominal two-dimensional charge current density calculated from the results; λ_s is spin diffusion length and θ_{sh} is the spin Hall angle of the chiral polymer; Supplementary Section III) as the figure of merit. We estimated the StC conversion length of the ICISS and ISHE responses in different chiral samples as summarized in Fig. 4a. Two features stand out. (1) The amplitude of the λ_{sc} value measured from both the ICISS and ISHE processes roughly scales with the carrier mobility (μ) in chiral polymers. It doesn't follow the change of SOC strength derived from the FMR measurements, which is supposed to be responsible for the StC conversion efficiency in heavy metals[46]. (2) The sign of the ICISS response is inverted upon the reversal of handedness in different polymers, whereas the ISHE counterpart does not change sign, implying two distinguishable StC conversion mechanisms in the two probe configurations.

The observed behaviours of spin lifetime ($\tau_s^{ISHE/ICISS}$), the conversion length λ_{sc}^{ICISS} and the electrical conductivity of chiral polymers can be correlated with the recently derived chirality-induced uSOC[47,48] and hopping transport in organic polymers. In a helical structure, the electron moves along a helix via hopping, which obeys the Dirac equation; it behaves the same as in a non-inertial system and acquires a finite acceleration according to relativity. Consequently, uSOC emerges as follows[47]:

$$H_{uSOC} = \sum_k \Omega(\alpha_{uSOC}\sigma_\Omega \cdot k_\Omega) \quad (2)$$

$$\alpha_{uSOC} = -\frac{tL^2r^2}{2\left[r^2+(\Delta d)^2\right]^{3/2}} \quad (3)$$

where σ_Ω and k_Ω are designated as the spin polarization and the wave vector along the chiral axis (the *y* axis in the experimental coordinate), and Ω is the handedness (Ω = +1 and −1 for R and S handedness, respectively); α_{uSOC} describes the strength of the uSOC; *r* and Δ*d* are the helix's radius and pitch, respectively; and *t* is the effective hopping interaction between nearest-neighbour sites at distance *L*. The uSOC lifts the spin degeneracy in the electronic structure, leading to the formation of one-dimensional spin-momentum-locking states (Fig. 4c). The band structures for up and down spins are represented by two parabolas, which are shifted in the k_Ω direction. The energy minimum, k_0, for up spin (σ_Ω = +1) and down spin (σ_Ω = −1) is no longer found at k_Ω = 0; this can be described as follows:

$$k_\Omega = \mp k_0 \equiv \mp\frac{\alpha_{uSOC}\Omega m_e}{\hbar^2} = \mp\frac{1}{4}\Omega\frac{r^2}{\left[r^2+(\Delta d)^2\right]^{3/2}} \quad (4)$$

which is determined entirely by the polymer's helical structural parameters, where m_e is the electron mass and $\hbar$ is the reduced Planck constant. The spin-up(down) electrons will occupy the outer spin-split band at $\pm k_\Omega$ for *R*(*S*) handedness. Upon spin injection, the spin polarization P_S causes an unbalanced population in the spin-up and spin-down bands. A finite current will be produced by a *k*-dependent spin-flip relaxation process since the spin-up band is more populated under the spin injection. The spin-flip transitions (determined by τ_s) from each parabola shown by the red and blue arrows in Fig. 4c are unbalanced due to the different momentum scattering rates ($1/\tau_p$), which creates an asymmetric carrier distribution around the minima in both parabolas. This asymmetric population results in a charge current flow, J_c^{ICISS}, along the chiral axis whose flow direction depends on Ω. Such a process shares similarities with the inverse Rashba–Edelstein effect, where the charge current generation depends on spin polarization ($\mathbf{J}_c \propto \mathbf{P}_S$) rather than a cross product of spin current flow and spin polarization via the ISHE process ($\mathbf{J}_c \propto \mathbf{J}_s \times \mathbf{P}_S$), as corroborated with the symmetry consideration. The generated current can be simply expressed as follows (further discussion in Supplementary Section VI):

$$J_c^{ICISS} \propto e n_e P_S \frac{\alpha_{uSOC}}{\hbar}\xi^2 \quad (5)$$

where *e*, n_e and ξ are the electron charge, electron density and spin admixture parameter due to the polymer's intrinsic SOC, respectively. This relationship suggests the conversion length, λ_{sc}^{ICISS}, is determined by the chirality-induced uSOC (α_{uSOC}) consistent with our experimental observations: the *S*-A device shows the largest structural chirality due to having the shortest pitches and helical radius, thereby possessing the strongest uSOC and damping factors (equation (3) and Supplementary Fig. 11). On the other hand, its ICISS efficiency is much smaller compared to that of the *R*-D device.

Moreover, we found that τ_s^{ISHE} and τ_s^{ICISS} are both inversely proportional to the mobility as shown in Fig. 4b, implying that the ICISS may have a similar hopping-relaxation process as found in most organic semiconductors. For the conventional spin transport in organic systems, the spin admixture parameter ξ plays a key role in the spin-flip process[49,50]. A linear relationship between τ_s^{ISHE} and mobility from the ISHE process (perpendicular to the chiral axis) is well described using the spin admixture ξ, which changes with the structural conformation, limiting the spin relaxation time $\tau_s^{ISHE} \approx 0.025 - 0.3$ ns in the ISHE process. A much longer spin lifetime when spin propagates along the chiral axis (τ_s^{ICISS}) may be directly attributed to a larger effective intermolecular hopping distance along the helical axis. Notably, the CISS occurs at $|k_\Omega| \leq k_0$. Thus, the ICISS effect manifests mainly around k_0 in the momentum space, corresponding to a length scale of $1/k_0$ that is much larger than the intermolecular hopping distance.

In summary, we have demonstrated the presence of the ICISS effect via spin-pumping techniques in a series of chiral conjugated polymers. The sign of the ICISS effect depends on the chirality of the polymers and this effect occurs solely when the injected spin polarization aligns with the chiral axis. It is attributed to an uSOC related to the structural-chirality-induced Berry curvature leading to a linear StC conversion. A chirality-driven spin relaxation is observed with respect to the chiral axis, exhibiting an unusually long spin lifetime of up to nanoseconds. Detailed descriptions of the uSOC and spin relaxation in the CISS/ICISS effect remain open. Our work provides a fertile ground for elucidating interplays of chirality and spin physics in organic-based chiral materials and launches the possibility of a variety of CISS-related spintronic, chemical, biological and quantum information applications using chiral assemblies of π-conjugated polymers.

Online content

Any methods, additional references, Nature Portfolio reporting summaries, source data, extended data, supplementary information, acknowledgements, peer review information; details of author contributions and competing interests; and statements of data and code availability are available at https://doi.org/10.1038/s41563-024-01838-8.

References

1. Wolf, S. A. et al. Spintronics: a spin-based electronics vision for the future. *Science* **294**, 1488–1495 (2001).
2. Soumyanarayanan, A., Reyren, N., Fert, A. & Panagopoulos, C. Emergent phenomena induced by spin–orbit coupling at surfaces and interfaces. *Nature* **539**, 509–517 (2016).
3. Hirohata, A. et al. Review on spintronics: principles and device applications. *J. Magn. Magn. Mater.* **509**, 166711 (2020).
4. Hirsch, J. E. Spin Hall effect. *Phys. Rev. Lett.* **83**, 1834–1837 (1999).
5. Kato, Y. K., Myers, R. C., Gossard, A. C. & Awschalom, D. D. Observation of the spin Hall effect in semiconductors. *Science* **306**, 1910–1913 (2004).
6. Saitoh, E., Ueda, M., Miyajima, H. & Tatara, G. Conversion of spin current into charge current at room temperature: inverse spin-Hall effect. *Appl. Phys. Lett.* **88**, 2199473 (2006).
7. Mosendz, O. et al. Detection and quantification of inverse spin Hall effect from spin pumping in permalloy/normal metal bilayers. *Phys. Rev. B* **82**, 214403 (2010).
8. Sun, D. et al. Inverse spin Hall effect from pulsed spin current in organic semiconductors with tunable spin–orbit coupling. *Nat. Mater.* **15**, 863–869 (2016).
9. Mosendz, O. et al. Quantifying spin Hall angles from spin pumping: experiments and theory. *Phys. Rev. Lett.* **104**, 046601 (2010).
10. Hoffmann, A. Spin Hall effects in metals. *IEEE Trans. Magn.* **49**, 5172–5193 (2013).
11. Sinova, J., Valenzuela, S. O., Wunderlich, J., Back, C. H. & Jungwirth, T. Spin Hall effects. *Rev. Mod. Phys.* **87**, 1213–1260 (2015).
12. Manipatruni, S. et al. Scalable energy-efficient magnetoelectric spin–orbit logic. *Nature* **565**, 35–42 (2019).
13. Pham, V. T. et al. Spin–orbit magnetic state readout in scaled ferromagnetic/heavy metal nanostructures. *Nat. Electron.* **3**, 309–315 (2020).
14. Grimaldi, E. et al. Single-shot dynamics of spin–orbit torque and spin transfer torque switching in three-terminal magnetic tunnel junctions. *Nat. Nanotechnol.* **15**, 111–117 (2020).
15. Ray, K., Ananthavel, S. P., Waldeck, D. H. & Naaman, R. Asymmetric scattering of polarized electrons by organized organic films of chiral molecules. *Science* **283**, 814–816 (1999).
16. Naaman, R. & Waldeck, D. H. Chiral-induced spin selectivity effect. *J. Phys. Chem. Lett.* **3**, 2178–2187 (2012).
17. Naaman, R., Paltiel, Y. & Waldeck, D. H. Chiral molecules and the electron spin. *Nat. Rev. Chem.* **3**, 250–260 (2019).
18. Göhler, B. et al. Spin selectivity in electron transmission through self-assembled monolayers of double-stranded DNA. *Science* **331**, 894–897 (2011).
19. Nakajima, R. et al. Giant spin polarization and a pair of antiparallel spins in a chiral superconductor. *Nature* **613**, 479–484 (2023).
20. Di Nuzzo, D. et al. High circular polarization of electroluminescence achieved via self-assembly of a light-emitting chiral conjugated polymer into multidomain cholesteric films. *ACS Nano* **11**, 12713–12722 (2017).
21. Kim, Y. H. et al. Chiral-induced spin selectivity enables a room-temperature spin light-emitting diode. *Science* **371**, 1129–1133 (2021).
22. Crassous, J. et al. Materials for chiral light control. *Nat. Rev. Mater.* **8**, 365–371 (2023).
23. Kiran, V. et al. Helicenes—a new class of organic spin filter. *Adv. Mater.* **28**, 1957–1962 (2016).
24. Bullard, G. et al. Low-resistance molecular wires propagate spin-polarized currents. *J. Am. Chem. Soc.* **141**, 14707–14711 (2019).
25. Kulkarni, C. et al. Highly efficient and tunable filtering of electrons' spin by supramolecular chirality of nanofiber-based materials. *Adv. Mater.* **32**, 1904965 (2020).
26. Banerjee-Ghosh, K. et al. Separation of enantiomers by their enantiospecific interaction with achiral magnetic substrates. *Science* **360**, 1331–1334 (2018).
27. Abendroth, J. M. et al. Spin selectivity in photoinduced charge-transfer mediated by chiral molecules. *ACS Nano* **13**, 4928–4946 (2019).
28. Chiesa, A. et al. Assessing the nature of chiral-induced spin selectivity by magnetic resonance. *J. Phys. Chem. Lett.* **12**, 6341–6347 (2021).
29. Aiello, C. D. et al. A chirality-based quantum leap. *ACS Nano* **16**, 4989–5035 (2022).
30. Chiesa, A. et al. Chirality-induced spin selectivity: an enabling technology for quantum applications. *Adv. Mater.* **35**, 2300472 (2023).
31. Inui, A. et al. Chirality-induced spin-polarized state of a chiral crystal $CrNb_3S_6$. *Phys. Rev. Lett.* **124**, 166602 (2020).
32. Diao, Y. et al. Solution coating of large-area organic semiconductor thin films with aligned single-crystalline domains. *Nat. Mater.* **12**, 665–671 (2013).
33. Diao, Y. et al. Flow-enhanced solution printing of all-polymer solar cells. *Nat. Commun.* **6**, 7955 (2015).
34. Park, K. S. et al. Tuning conformation, assembly, and charge transport properties of conjugated polymers by printing flow. *Sci. Adv.* **5**, eaaw7757 (2019).
35. Park, K. S., Kwok, J. J., Kafle, P. & Diao, Y. When assembly meets processing: tuning multiscale morphology of printed conjugated polymers for controlled charge transport. *Chem. Mater.* **33**, 469–498 (2021).

36. Park, K. S. et al. Chiral emergence in multistep hierarchical assembly of achiral conjugated polymers. *Nat. Commun.* **13**, 2738 (2022).
37. Wittmann, A. et al. Tuning spin current injection at ferromagnet-nonmagnet interfaces by molecular design. *Phys. Rev. Lett.* **124**, 027204 (2020).
38. Vetter, E. et al. Tuning of spin-orbit coupling in metal-free conjugated polymers by structural conformation. *Phys. Rev. Mater.* **4**, 085603 (2020).
39. Azevedo, A., Vilela-Leão, L. H., Rodríguez-Suárez, R. L., Lacerda Santos, A. F. & Rezende, S. M. Spin pumping and anisotropic magnetoresistance voltages in magnetic bilayers: theory and experiment. *Phys. Rev. B* **83**, 144402 (2011).
40. Calavalle, F. et al. Gate-tuneable and chirality-dependent charge-to-spin conversion in tellurium nanowires. *Nat. Mater.* **21**, 526–532 (2022).
41. Qian, Q. et al. Chiral molecular intercalation superlattices. *Nature* **606**, 902–908 (2022).
42. Ando, K. & Saitoh, E. Observation of the inverse spin Hall effect in silicon. *Nat. Commun.* **3**, 629 (2012).
43. Wang, S.-J. et al. Long spin diffusion lengths in doped conjugated polymers due to enhanced exchange coupling. *Nat. Electron.* **2**, 98–107 (2019).
44. Yu, Z. G. Spin Hall effect in disordered organic solids. *Phys. Rev. Lett.* **115**, 026601 (2015).
45. Sun, R. et al. Visualizing tailored spin phenomena in a reduced-dimensional topological superlattice. *Adv. Mater.* **32**, 2005315 (2020).
46. Chen, K. & Zhang, S. Spin pumping in the presence of spin-orbit coupling. *Phys. Rev. Lett.* **114**, 126602 (2015).
47. Yu, Z. G. Chirality-induced spin–orbit coupling, spin transport, and natural optical activity in hybrid organic–inorganic perovskites. *J. Phys. Chem. Lett.* **11**, 8638–8646 (2020).
48. Shitade, A. & Minamitani, E. Geometric spin–orbit coupling and chirality-induced spin selectivity. *New J. Phys.* **22**, 113023 (2020).
49. Yu, Z. G. Spin-orbit coupling, spin relaxation, and spin diffusion in organic solids. *Phys. Rev. Lett.* **106**, 106602 (2011).
50. Yu, Z. G. Spin-orbit coupling and its effects in organic solids. *Phys. Rev. B* **85**, 115201 (2012).

Publisher's note Springer Nature remains neutral with regard to jurisdictional claims in published maps and institutional affiliations.

Springer Nature or its licensor (e.g. a society or other partner) holds exclusive rights to this article under a publishing agreement with the author(s) or other rightsholder(s); author self-archiving of the accepted manuscript version of this article is solely governed by the terms of such publishing agreement and applicable law.

© The Author(s), under exclusive licence to Springer Nature Limited 2024

Methods

Materials

The isoindigo-based copolymer PII2T (number-averaged molecular weight = 30,645 g mol^{-1}, weight-averaged molecular weight = 76,809 g mol^{-1} and polydispersity index = 2.50) was synthesized as previously described[51]. The solution was prepared by dissolving the polymer (10 mg ml^{-1}) in chlorobenzene (anhydrous, 99.8%, Sigma-Aldrich). Corning glass substrates were used as substrates. The substrates were cleaned with toluene, acetone and isopropyl alcohol, and then blow-dried with a stream of nitrogen to remove contaminants. A heavily doped n-type Si with a 300-nm-thick, thermally grown SiO_2 layer was used as an oxide substrate for the field-effect transistors. The surfaces of the SiO_2 substrates were modified by a hydrophobic self-assembled monolayer treatment. The self-assembled monolayer treatment was achieved by immersing the plasma-activated substrates in a dilute solution (0.1 vol%) of *n*-octyldecyltrichlorosilane (OTS; Acros, 95%) with trichloroethylene (anhydrous, >99.5%, Sigma-Aldrich) at room temperature for 20 min. The treated substrates were then rinsed with toluene, dried with nitrogen and annealed at 120 °C for 20 min.

Device fabrications

PII2T thin films were printed onto substrates by a meniscus-guided printing method such as blade coating. The blade coating method was reported in our previous publication[34]. Briefly, an OTS-treated Si substrate was used as a blade set at an angle of 7°, with a gap of 100 µm between the substrate and the blade. The blade was linearly translated over the stationary substrate while retaining the ink solution within the gap. The PII2T films were prepared on a bare Corning glass or OTS-treated SiO_2 substrates at printing speeds of 2.5 µm s^{-1} (*S*-A sample), 5 µm s^{-1} (*S*-B sample), 6 µm s^{-1} (*R*-C sample) and 50 µm s^{-1} (*R*-D sample) with a substrate temperature of 25 °C. The $Ni_{81}Fe_{19}$ layer was deposited at room temperature using electron-beam evaporation with a chamber base pressure of 1×10^{-6} torr and evaporation rate of 0.25 Å s^{-1}.

Printed film characterization. The birefringence of the PII2T polymer films was characterized using cross-polarized optical microscopy (Nikon Eclipse Ci-POL). The mesoscale morphology was characterized using tapping mode atomic force microscopy (Asylum Research Cypher). UV–visible (Cary 60 UV-Vis, Agilent) spectroscopy was used to measure the absorption of films. Grazing-incidence wide-angle X-ray scattering measurements were performed at beamline 8-ID-E at the Argonne National Laboratory, with an incident beam energy of 7.35 keV on a two-dimensional detector (PILATUS 1M) at a 208 mm sample-to-detector distance. Samples were scanned for 10 s in a helium chamber. The X-ray incident angle was set to be above (0.14°) the critical angle (~0.1°) of the polymer layer (penetration depth, ~5 nm). CD were recorded using a JASCO 1500 spectrophotometer. All electrical measurements were performed in a nitrogen environment using a Keysight B1500A semiconductor parameter analyser.

FMR and spin-pumping measurements. For the FMR measurements, the samples were mounted on a coplanar waveguide (NanOsc). The microwaves were generated by a Keysight X-series microwave analog signal generator, whose frequency *f* is the resonance frequency for the FMR condition. The *f* value is in the range of 2–18 GHz while the generated radio-frequency field h_{rf} lies in the film plane. For the spin-pumping voltage detection, the resonance frequency *f* was fixed at 6 GHz, while the ISHE/ICISS voltage was modulated by modulating the microwave power at f_{mod} = 233 Hz (a sine wave) as described elsewhere for the spin-pumping technique. The ISHE/ICISS voltage was recorded using a Stanford lock-in amplifier[45]. The $V^{ISHE/ICISS}$ was obtained via $V^{ISHE/ICISS} = V_S(+H) - V_S(-H)$ in the calculation of λ_{sc} and Hanle curves. The electrodes were attached on the device, parallel or perpendicular to the chiral axis as shown in Fig. 2. In the ICISS configuration detection, the electrodes were parallel to **H**, while they were perpendicular to **H** for the ISHE configuration detection. The magnetic field **H** can be applied to an out-of-plane angle θ for the spin Hanle effect measurement. All the measurements were performed at room temperature.

Data availability

All data in the main text or the Supplementary Information is available upon reasonable request. Source data are provided with this paper.

References

51. Lei, T., Dou, J.-H. & Pei, J. Influence of alkyl chain branching positions on the hole mobilities of polymer thin-film transistors. *Adv. Mater.* **24**, 6457–6461 (2012).

Acknowledgements

D.S., Y.D., A.H., W.Y., D.B. and P.Z. acknowledge financial support from the Air Force Office of Scientific Research, Multidisciplinary University Research Initiatives (MURI) programme under award number FA9550-23-1-0311. Device fabrication at NC State University was partially supported by the Department of Energy under award number DE-SC0020992 and the National Science Foundation under award DMR-2143642. Y.D. acknowledges financial support from the National Science Foundation under award DMR-1847828 and partial support by the Office of Naval Research under award number N00014-2220-1-2202. W.Y. acknowledges financial support from the Office of Naval Research under award number N00014-20-1-2181. Z.-G.Y. acknowledges financial support by the US Air Force (FA9550-22-P-0014). A.H. acknowledges financial support from the Illinois Materials Research Science and Engineering Center, supported by the National Science Foundation Materials Research Science and Engineering Centers (MRSEC) programme under National Science Foundation award no. DMR-1720633.

Author contributions

D.S., Y.D. and R.S. conceived the experiment and supervised this research. R.S. and K.S.P. were responsible for the spin and electron transport measurements. K.S.P., R.S., A.H.C., A.M. and Y.-C.C. fabricated the samples. Z.-G.Y. provided the theoretical models. R.S., P.Z., D.B., W.Y. and A.H. conducted the spin transport analysis. R.S. and D.S. wrote the paper. All authors contributed to editing the paper.

Competing interests

The authors declare no competing interests.

Additional information

Supplementary information The online version contains supplementary material available at https://doi.org/10.1038/s41563-024-01838-8.

Correspondence and requests for materials should be addressed to Ying Diao or Dali Sun.

Peer review information *Nature Materials* thanks the anonymous reviewers for their contribution to the peer review of this work.

Reprints and permissions information is available at www.nature.com/reprints.